Review Article

Omar Rodríguez-Núñez and Tatiana Novikova*

Polarimetric techniques for the structural studies and diagnosis of brain

Abstract: The polarimetric techniques are used in various biomedical applications for a non-contact and fast diagnosis of tissue that is known as optical biopsy approach. These optical modalities provide relevant information on micro-architecture of biological tissue and its alterations induced by different diseases, thus, helping in staging and precise delineation of the pathology zones. In this review, we summarize the work of different research groups on using polarized light for brain tissue studies. This includes the investigations of polarimetric properties of brain tissue (both scattering and optical anisotropy) for brain connectome reconstruction, the visualization of in-plane brain fiber tracts for brain tumor contrast enhancement during neurosurgery, and the histopathology analysis for disease staging in Alzheimer's subjects. We discuss also further perspectives for the pre-clinical studies of brain with polarized light.

Keywords: brain connectome; brain pathology; optical anisotropy; optical polarization; scattering; white matter of brain.

1 Introduction

Brain is the most complex organ in a body of any vertebrate and brain structure reflects the complexity of its multiple functions. The outer shell of a brain (i.e. cortex, or gray matter) includes billions of neuron cell bodies that are inter-connected by axons serving for a transfer of nerve impulses. Axons are packed in the bundles (or fiber tracts) that constitute white matter inside the brain together with the different types of supporting and protective cells that assure reliable and correct functioning of the brain.

The different functional activities (e.g. vision, speech, voluntary movements, etc.) are supported by the specific brain fiber tracts. Mapping the neuron connections (so called brain connectome) helps to understand the foundation of human cognition because the dynamic interactions between the neurons are shaped by the brain connectome. The transformations of brain tissue by pathology (e.g. Alzheimer's disease, brain tumors, etc.) may strongly affect the brain connectivity by modifying or destroying healthy brain fiber tracts.

Since long time the different optical modalities are explored for the studies of structural and functional properties of the brain. These studies span over the large range of domains from fundamental optics to clinical applications. In this paper, we provide a concise overview of the polarimetric techniques that explore the sensitivity of polarized light to the anisotropy of the refractive index of healthy brain white matter and demonstrate their potential for various applications.

Light is a transverse electromagnetic wave in general (if viewed classically), with the oscillating electric and magnetic fields being perpendicular to each other as well as to the direction of wave propagation. Apart from the intensity that represents a fundamental scalar property of light, polarization describes its vectorial nature. Light can be emitted by different sources, and scattered by a medium or object. The state of polarization of light provides information about the emitting sources and scattering media. Optical polarimetry, which studies the mechanisms for measuring the polarization state of light, has contributed to different areas of science such as physics, chemistry, and biology. In addition, it has provided essential diagnostic, sensing, analytical, and metrology tools in numerous applications, including the biomedical, pharmaceutical, and microelectronics industries, among others [1].

The polarization properties of an object, as well as the polarization state of a light beam, can be described in different ways. One possibility is to represent the linear system with a matrix and both probing and detected light

*Corresponding author: Tatiana Novikova, LPICM, CNRS, Ecole polytechnique, IP Paris, Palaiseau 91128, France,
E-mail: tatiana.novikova@polytechnique.edu. https://orcid.org/0000-0002-9048-9158
Omar Rodríguez-Núñez, LPICM, CNRS, Ecole polytechnique, IP Paris, Palaiseau 91128, France,
E-mail: omar.rodriguez-nunez@polytechnique.edu

beams with the vectors. The interaction of the incident light beam with an object is then represented by the product of the corresponding matrix and vector. Jones formalism [2] is a suitable framework to describe this interaction using 2×2 complex-valued Jones matrix of an object and two complex components of the Jones vector as long as this object is a non-depolarizing one. A more general formalism is given by the combination of the 4×4 real-valued Mueller matrix of an object and four real components of the Stokes vector of a beam [1–3]. In 1852, Sir George Stokes discovered that polarized light could be described in terms of the observables. He found that any polarization state of a light beam for completely polarized, partially polarized and unpolarized light, could be represented in terms of four measurable quantities, that are now known as the Stokes parameters, i.e. the elements of the Stokes vectors. For quasi-monochromatic light the definition of the Stokes vector [3, 4] reads as

$$\mathbf{S} = \begin{bmatrix} S_0 \\ S_1 \\ S_2 \\ S_3 \end{bmatrix} = \begin{bmatrix} \langle E_x E_x^* + E_y E_y^* \rangle \\ \langle E_x E_x^* - E_y E_y^* \rangle \\ \langle E_x E_y^* + E_y E_x^* \rangle \\ i \langle E_x E_y^* - E_y E_x^* \rangle \end{bmatrix} = \begin{bmatrix} \langle E_{0x}^2 + E_{0y}^2 \rangle \\ \langle E_{0x}^2 - E_{0y}^2 \rangle \\ \langle 2E_{0x}E_{0y}^2 cos\delta \rangle \\ \langle 2E_{0x}E_{0y}^2 cos\delta \rangle \end{bmatrix}, \quad (1)$$

where E_x and E_y are the components of the electric field in the x- and y-direction, respectively. The symbol $\langle \rangle$ indicates that the quantities are ensemble averages but, assuming the stationarity and ergodicity, they can be replaced by time averages with the same result. The first element S_0 of the Stokes vector is the total irradiance, the second one S_1 is the fraction of light linearly polarized in the horizontal and/or vertical direction, the third element S_2 is the fraction linearly polarized at ±45°, and the fourth one S_3 is the fraction of light circularly polarized with right or left handedness.

The Stokes parameters enable us to describe the degree of polarization DOP for any light beam as

$$DOP = \frac{I_{pol}}{I_{tot}} = \frac{\sqrt{S_1^2 + S_2^2 + S_3^2}}{S_0}, \quad 0 \le DOP \le 1, \quad (2)$$

where I_{pol} is the intensity of sum of the polarization components and I_{tot} is the total intensity of a beam. The value of DOP = 1 corresponds to completely polarized light, DOP = 0 corresponds to unpolarized light, and 0 < DOP < 1 corresponds to partially polarized light. Using Stokes vector components that describe the intensity of linearly polarized and circularly polarized fractions of a light beam we can define the degree of linear polarization and degree of circular polarization of light, respectively:

$$DOLP = \frac{\sqrt{S_1^2 + S_2^2}}{S_0}, \quad (3)$$

$$DOCP = \frac{S_3}{S_0}, \quad (4)$$

Since the degree of polarization of light cannot exceed unity, the Stokes parameters have to obey the restriction, $S_0 \ge \sqrt{S_1^2 + S_2^2 + S_3^2}$ [2–5]. Mueller matrix M transforms a Stokes vector of light impinging on a sample into another Stokes vector of light emerging from a sample [3, 6]. The Mueller matrix contains all information concerning the polarization properties of an object that this matrix represents (e.g. diattenuation, phase retardance, and depolarization) [2, 3]. The transformation of an incident wave with a Stokes vector $\mathbf{S}^{in}$ into a wave with a Stokes vector $\mathbf{S}^{out}$ can be described by

$$\mathbf{S}^{out} = \mathbf{M} \cdot \mathbf{S}^{in}, \quad (5)$$

$$\begin{bmatrix} S_0^{out} \\ S_1^{out} \\ S_2^{out} \\ S_3^{out} \end{bmatrix} = \begin{bmatrix} M_{00} & M_{01} & M_{02} & M_{03} \\ M_{10} & M_{11} & M_{12} & M_{13} \\ M_{20} & M_{21} & M_{22} & M_{23} \\ M_{30} & M_{31} & M_{32} & M_{33} \end{bmatrix} \begin{bmatrix} S_0^{in} \\ S_1^{in} \\ S_2^{in} \\ S_3^{in} \end{bmatrix}. \quad (6)$$

Depending on the polarization properties of the object, there may be the symmetries between the elements of Mueller matrix. However, in the most general case, all the elements of the matrix are different. An important property of the Mueller matrix representation of polarization is linearity. That is, the total effect over the polarization of a light beam due to a series of N optical elements, each one represented by a Mueller matrix M_i, $i = 1, \ldots, N$, is given by

$$\mathbf{M} = \mathbf{M}_N \cdots \mathbf{M}_2 \mathbf{M}_1. \quad (7)$$

In Eq. (7), $\mathbf{M}_1$ is the Mueller matrix of the first-to-be-encountered optical element along the light-beam path.

A complete Mueller matrix polarimeter is always composed of a polarization-state generator (PSG) that generates at least four linearly independent basis states $\mathbf{S}^{in}$, and a polarization state analyzer (PSA) that also generates at least four linearly independent basis polarization states to which the corresponding Stokes vector of emerging $\mathbf{S}^{out}$ is projected. For a single-channel system a PSG generates exactly four St vectors $\mathbf{S}^{in}$ that form the columns of the modulation matrix, $\mathbf{W}$. Similarly, the PSA is assumed to project $\mathbf{S}^{out}$ over exactly four St vectors that form the rows of the analyzer matrix, $\mathbf{A}$. Then, a complete set of 16 measurements of a sample characterized by a Mueller matrix $\mathbf{M}$ can be written in a matrix form as:

$$\mathbf{B} = \mathbf{AMW}, \tag{8}$$

and $\mathbf{M}$ can be extracted readily from the measured raw intensity matrix $\mathbf{B}$, provided that $\mathbf{A}$ and $\mathbf{W}$ are known, i.e., if the system is calibrated [5]. Light polarization can be modulated and analyzed by using a variety of optical components and approaches: rotating retardation plates [1, 7], rotating compensators [8], Pockels cells [9], photoelastic modulators [10, 11], or liquid-crystal variable retarders [12, 13]. The straightforward physical interpretation of the elements of Mueller matrix is possible for quite limited class of samples. In general case, one needs to apply one of the non-linear data compression algorithms also known as the decompositions of Mueller matrix that provide the polarimetric properties of a sample – dichroism, retardance, and depolarization [14–17]. The techniques that measure only some of Mueller matrix elements are called partial polarimetric techniques. For the samples with *a priori* known polarimetric properties it can be beneficial to use partial Stokes polarimetry because of simpler instrument design.

2 Partial polarimetric techniques for imaging brain fiber tracts

2.1 Transmission configuration

It is well known that using images obtained through polarized light microscopy, anisotropic structures can be studied in histological sections [18, 19]. Typically, a polarizer is inserted into the illumination arm, then a second polarizer (so-called analyzer) is placed in the detection arm after light beam passes through a sample. The transmission axes of both linear polarizers are required to be oriented orthogonal to each other. When a sample represents anisotropic scattering medium, the orientation of the polarization plane of probing light beam will change, so some part of radiation will pass through an analyzer and can be detected. Therefore, the fraction of light that passes through the analyzer depends on the orientation of the anisotropic structures within the sample with respect to the transmission axes of both polarizers that make up the system [20].

In particular, for the polarimetric imaging of fibers of a central nervous system in thin sections of brain, there are two relevant parameters: birefringent properties of nervous tissue and thickness of tissue section. Nervous fibers produce a negative birefringence that is associated with the presence of oriented lipids in the myelin sheaths of axons.

Hence, polarized light allows visualization of the orientation of nerve fiber tracts [20–23].

In 2001, Axer et al. [24] described the polarized light imaging (PLI) instrument operating in transmission configuration and consisting of two rotating, mutually orthogonal, polarizers, and a quarter-wave plate (QWP). Figure 1 illustrates PLI experimental setup and its operating principles for mapping in-plane orientation and inclination angle of brain nerve fibers within thin histological sections of brain tissue [24, 25]. White matter of brain contains densely packed bundles of nerve fibers (myelinated axons) and represents linearly birefringent medium with its slow optical axis aligned with fiber tract direction.

The optical axes of a QWP (placed between two polarizers and a sample) are fixed at 45° with respect to the transmission axes of two crossed polarizers. Linearly polarized light passing through a birefringent sample is transformed into elliptically polarized light. The fraction of transmitted elliptically polarized light depends on the orientation of the ellipse axes relatively to the axes of optical elements in the detection arm. Both birefringent sample (e.g. a section of brain tissue) and QWP act as retarders. Hence, the position of a QWP with respect to a birefringent sample is not critical, and a QWP can be inserted either before or after the sample. To estimate the transmitted light intensity the Jones calculation [28] is used: $I_{\text{trans}} = \frac{1}{2}I(1 + \sin\delta\sin(2(\rho - \varphi)))$, where δ represent the phase difference associated with birefringence and thickness of brain tissue section. Then, ρ and φ represent the azimuth angles of the transmission axis of the first polarizer and the in-plane direction of individual fiber, respectively, in a laboratory reference frame.

Transmitted intensity images were recorded with PLI for thin histological sections of corpus callosum of formalin-fixed human brain at different rotation angles of polarizers. The angular spectra of transmitted intensity were used for a quantitative estimation of inclination angle (z-direction) and direction angle (in the xy-plane) of brain fiber tracts. For the sections with optimal thickness of 100 μm and nominal fiber inclination angle varying between 0° and 90°, a linear relationship was established between the maximum of detected intensity values and the nominal value of fiber inclination angle as cut by a pathologist. This linear regression curve was used as a calibration curve for the estimation of fiber inclination angle. Minimum value of angular-dependent transmitted intensity measured with two rotating polarizers and an inserted QWP provided unambiguously the direction angle of brain fibers in xy plane.
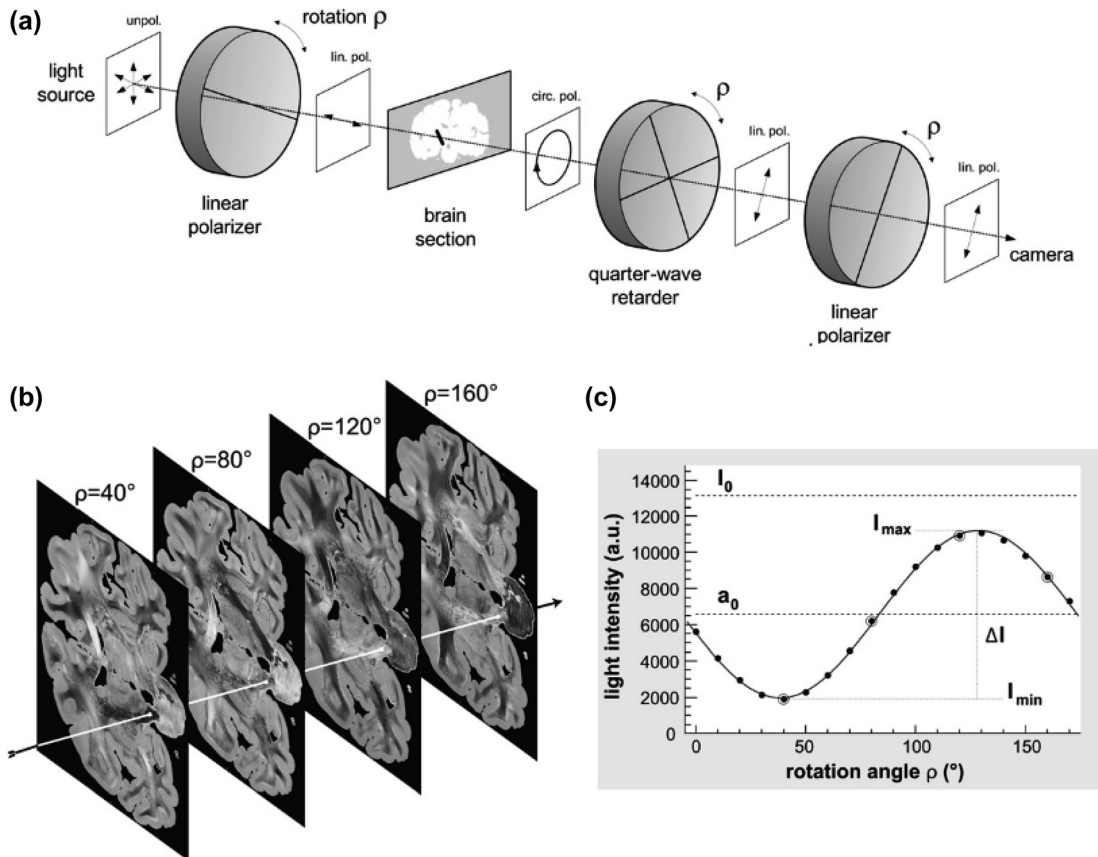
Figure 1: Image acquisition. (a) Scheme of the custom-built rotating polarimeter. The optical components of the setup modulate the polarization state of transmitted light in a defined manner [26]. To illustrate the changes in light beam polarization, the trajectory of electric field vector is highlighted by arrows at fixed positions after each optical component. As an example – an in-section brain fiber is acting as an ideal quarter-wave retarder. (b) A whole brain section is imaged at 18 different rotation angles ranging from 0° to 170°. The sketched arrow indicates one representative pixel. (c) To obtain local fiber orientations from the series of PLI raw intensity images, the measured light intensities are studied pixel-wise as a function of discrete rotation angles (light intensity profile). The prediction of theoretical model is shown by the solid line. The open circles represent the measured intensities of the corresponding pixels selected within the PLI images in (b). Reproduced with the permission from [27].

Using the results of these measurements and the calibration curves, the fiber orientation maps in gross histological sections of the human brain were calculated, similar to the fiber orientation maps produced in diffusion-weighted magnetic resonance imaging. The maps of fiber inclination were estimated within a range from 0° to 90° and the maps of fiber direction varied within a range from 0° and 180°. The former is due to the fact that PLI technique detects the same transmitted intensity for the fibers with inclination angles that are symmetric with respect to the imaging plane (for example +45° and −45°), so they cannot be distinguished.

Diffusion tensor magnetic resonance imaging (DT-MRI) modality tracks three dimensional (3D) orientation of nerve fiber tracts in living human brain by measuring anisotropy of water diffusion [29]. The reconstruction of 3D fiber model of a human brainstem with PLI of serial

gross histological sections of post-mortem human brain was demonstrated by Axer et al. [30]. Both fiber orientation and inclination maps of human brainstem histological sections (100 μm nominal thickness) were generated first. Then both orientation (xy plane) and inclination (z direction) maps were transformed into an array of unit vectors with x-, y- and z-coordinates. To visualize 3D fiber orientation in one 2D image these coordinates were R-, G-, B-color-coded. The automatic alignment of RGB images of the adjacent sections was performed using minimization of Euclidean distance in the intensity space. To resolve the ambiguity for the inclination angle close to ±45° Larsen et al. [31] made use of fiber tracts continuity. At each image pixel the inclination angle was chosen to assure a slow spatial variation in fiber orientation over the reconstructed volume. The aligned RGB images were imported into the software 3D Slicer that generated 3D reconstruction of the

fiber anatomical structures of brainstem with higher spatial resolution compared to DT-MRI modality.

Another important neuroanatomical study of the visualization of nerve fiber tracts orientation within white matter of human brain is presented in [32]. The PLI system was tested with histological sections of the visual cortex of human brain. The orientation and intensity maps recorded for each brain section were used for 3D reconstruction of brain fiber tracts that provided the insights into large-distance connectivity of functional brain areas through fiber tracking. The higher spatial resolution of the PLI technique represents its main strength compared to DT-MRI for mapping the structure of individual sections of brain fibers. Consequently, the PLI maps may serve as a complementary neuroanatomical method for the validation of DT-MRI maps.

The crossing of different fibers on a sub-millimeter scale represented the real challenge for fiber tracking by DT-MRI techniques [33, 34], mainly due to their low spatial resolution. In 2011 Axer et al. [27] proposed a 3D-Polarized Light Imaging (3D-PLI) method by defining an isotropic voxel with the dimensions no larger than 100 μm × 100 μm × 100 μm. This imaging modality allows to map the 3D course of fiber tracts of a human brain with sub-millimeter-scale resolution even in brain regions with the dense fiber crossing.

The maps of PLI parameters of a whole brain section in coronal plane are shown in Figure 2. The image of light intensity I transmitted at the rotation angle ρ is shown in Figure 2a. The analysis of transmitted light intensity profile measured at different rotation angles ρ at each pixel of the image allows to extract the set of PLI parameters. The retardation map $|\sin \delta|$ (Figure 2b) provides information about the angle α of fiber inclination. The map of angle α is calculated using following relation $\delta \approx 2\pi(\frac{d\Delta n}{\lambda})\cos^2\alpha$, provided that measurement wavelength λ, local birefringence Δn and section thickness d are known. The map of fiber direction angles φ is obtained from the fit of intensity profile [27]. The corresponding maps of α and φ representing the inclination and direction of nerve fiber tracts are shown in Figure 2c, d, respectively.

3D mapping of the nerve fibers and fiber tracts of an adult human brain presented by Axer et al. [27] allows to increase the resolution, reaching a degree of details an order of magnitude superior to the DT-MRI tractography. Unlike the dissection or myelin staining techniques used for the study of fiber tracts in post-mortem brains [35–37], the mapping of fiber tract with 3D PLI modality has the advantage of reaching sub-millimeter resolution.
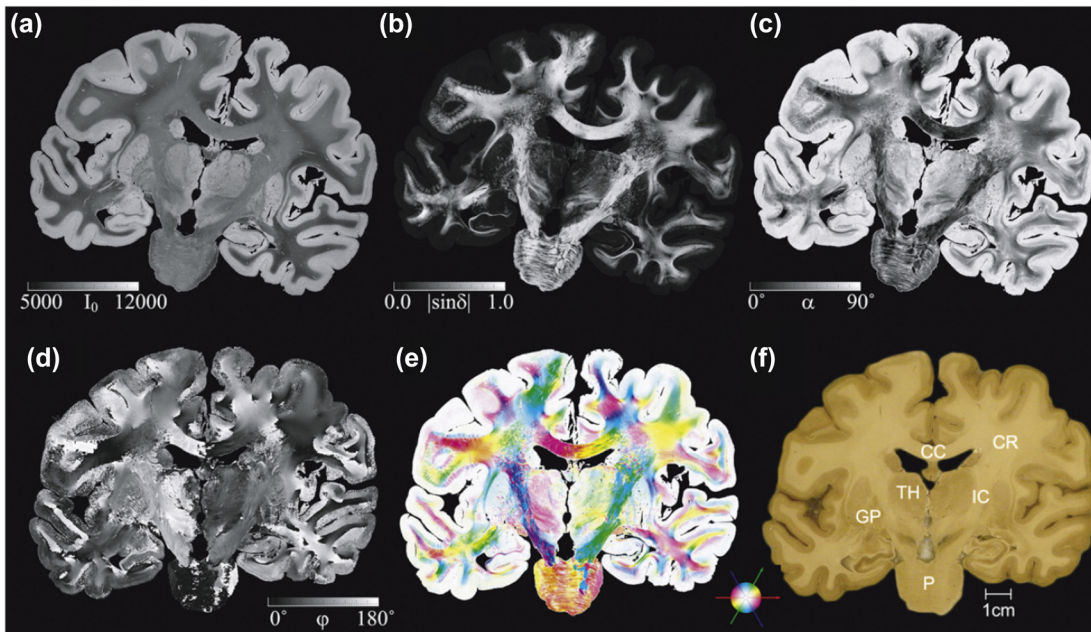

Figure 2: PLI parameter maps of coronal whole brain section: (a) Transmittance I_0; (b) retardation $|\sin\delta|$; (c) fiber inclination α; (d) fiber direction φ; (e) fiber orientation comprising both inclination and direction information. The latter is visualized in HSV color space, i.e. the color encodes φ and the saturation defines α from saturated color ($\alpha = 0°$) to white ($\alpha = 90°$). Transversal fibers are colored in red (see color sphere); (f) the associated blockface image served as alignment reference: CC — corpus callosum, CR — corona radiata, IC — internal capsule, TH — thalamus, GP — globus pallidus, P — pons. Reproduced with the permission from [27].

The PLI modality, developed and described in [24, 27, 31, 32] was used for the study of human brain connectome [38]. The original 3D-PLI system was upgraded by using a multi-scale approach that allows both microscopic and macroscopic characterization of anatomical connectivity through the use of different polarimetric configurations. Taking the PLI measurements at various angles of sample tilt helped to address the ambiguity of fiber inclination angles close to ±45°. The capability of upgraded system to detect small myelinated fiber tracts within the cerebral cortex was demonstrated. Also, the versatility of multi-scale polarimetric data allowed the analysis of fibers orientation with both 2D and 3D images, thus, helping in tracking the specific fiber tracts through the regions of crossing and kissing fibers.

The 3D-PLI modality was used for the study of connections between language-related areas and the anatomy of fibers related to language in both human and monkey brains with special focus on the ventral stream [39]. A clear correlation was found between the architecture of brain white matter tracts connecting language-related areas for both dorsal and ventral language streams. A significant difference between the fiber architecture in human and monkey brains was identified in the same study.

In [40] Menzel et al. discussed the validity of the uni-axial negative birefringence model for brain white tissue that was used in the 3D-PLI for fiber tracking. The numerical simulations based on the Jones matrix calculation [28] and using either macroscopic model of brain white tissue (slow optical axis is aligned with nerve fiber direction) or the microscopic model (radial optical axes related to the arrangement of the molecules of lipids within myelin sheath of an axon) demonstrated that 3D-PLI measurements are described correctly by former model when spatial resolution of the polarimetric system is larger than the size of an individual nerve fiber.

In [40], a straight parallel nerve fiber arrangement is analyzed only, whereas Dohmen et al. [41] have also simulated the effect of fiber crossing. They demonstrated that crossing fibers as well as different densities of myelin within crossing fibers perturb the correct reconstruction of fiber orientation with 3D-PLI modality. The accuracy of the reconstruction can be improved by performing 3D-PLI measurements at different tilt angles of a specimen. Using a tiltable sample stage for the evaluation of the out-of-plane fiber inclination was also suggested by Schmitz et al. [42].

2.2 Reflection configuration

Recently Jain et al. [43] investigated the local structural anisotropy of a thick section of a formalin-fixed human

brain with Mueller microscope operating in reflection configuration. They demonstrated that a method of the analysis of Stokes vector components is capable to detect the birefringence exhibited by brain white matter and relate it to the fiber orientation and the degree of fiber alignment. The design of the imaging polarimeter used in [43–45] is similar to the design of Mueller microscope described in [46, 47]. The schematic of optical layout of the imaging polarimetric setup is shown in Figure 3.

The instrument is composed of the illumination arm that contains a polarization state generator (PSG) for polarization modulation of the incident beam, and the detection arm that includes a two-lens system for detection and a polarization state analyzer (PSA) for the analysis of polarization state of the reflected beam. A PSG consists of a linear polarizer and two liquid crystal variable retarders (LCR). The fast axis of the first retarder is oriented at $\pi/4$ with respect to the x- and y-axes of the lab frame, whereas the fast axis of the second retarder is aligned with the y-axis in the laboratory reference frame. A PSA consists of the same elements, but assembled in a reverse order. A tunable super continuum laser with a wavelength span from 480 to 900 nm was used as a light source. The collimated light beam passed through a PSA followed by a non-polarizing beam-splitter cube and focusing lens before illuminating surface of a sample. The backscattered light was also collected by the same focusing lens after interacting with a sample. Backscattered light goes through a beam-splitter
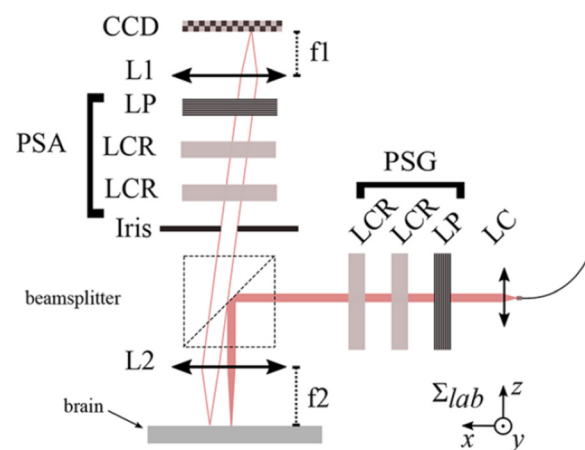

Figure 3: Schematic drawing of the imaging polarimetric setup. PSG – polarization state generator, PSA – polarization state analyzer. LC, L1, and L2 designate lenses. LCR and LP are liquid crystal retarders and linear polarizers, respectively. The scattering system is probed at $\lambda = 785$ nm by a focused beam. The spatial distribution of the backscattered light intensity is recorded by a CCD chip placed at the end of the detection arm. Σ_{lab} denotes the laboratory reference frame. Reprinted with permission from [43]. ©The optical Society.

and two-lens system. An iris placed in a back focal plane of the first lens determines the numerical aperture of the imaging system. A PSA is placed between two lenses that are followed by CCD camera for the detection of a backscattered image.

Using the experimental setup described above, the spatially dependent Mueller matrices of anisotropic fibrous phantoms were recorded by Jain et al. [45], and, subsequently, the backscattered Stokes vector images were reconstructed for six incident polarization states of probing beam (linear horizontal, linear vertical, linear ±45°, left and right circular) by multiplying the corresponding Stokes vector of incident light by the measured Mueller matrices. Then the four polarization ellipse parameters (orientation, ellipticity, helicity and degree of polarization) [5, 44, 45] were calculated using the elements of Stokes vector. It was shown that the linear polarization state of a probing beam is most preserved when the orientation of polarization plane is parallel or perpendicular to the optical axis of linear birefringent medium. The degree of linear polarization [48] can be used for the determination of the degree of alignment of fibrous materials. It also provides a most intuitive metrics of the degree of micro-structural alignment in tissue [43].

By analyzing the spatial distribution of degree of polarization of diffuse backscattered light and its variation as a function of input polarization state of a weakly focused probing light beam Jain et al. [43] distinguished between two structurally different brain tissue types, namely, gray and white matter (see Figure 4).

Jain et al. [43] reported that estimated mean alignment directions found in brain white matter with the polarimetric microscopy are in a good agreement with the brain nerve fibers pathways [49, 50]. The analysis of different regions in Figure 4 highlights the gradual transition from highly aligned zones to regions with lower degree of alignment related to fibers crossing and inclination.

Jain et al. [43] suggested that the described polarized microscopy technique holds promise for *in-vivo* detection of the degree of fiber alignment in healthy brain tissue without prior tissue preparation and could serve for accurate identification of vital nerve fiber tracts during neurosurgery.

3 Complete Mueller polarimetry in reflection geometry

Wide-field imaging complete Mueller matrix polarimetry has demonstrated its potential for optical diagnosis of cervical intraepithelial neoplasia [51, 52], colon cancer [53, 54], preterm birth risk [55], staging of Alzheimer's disease [56]
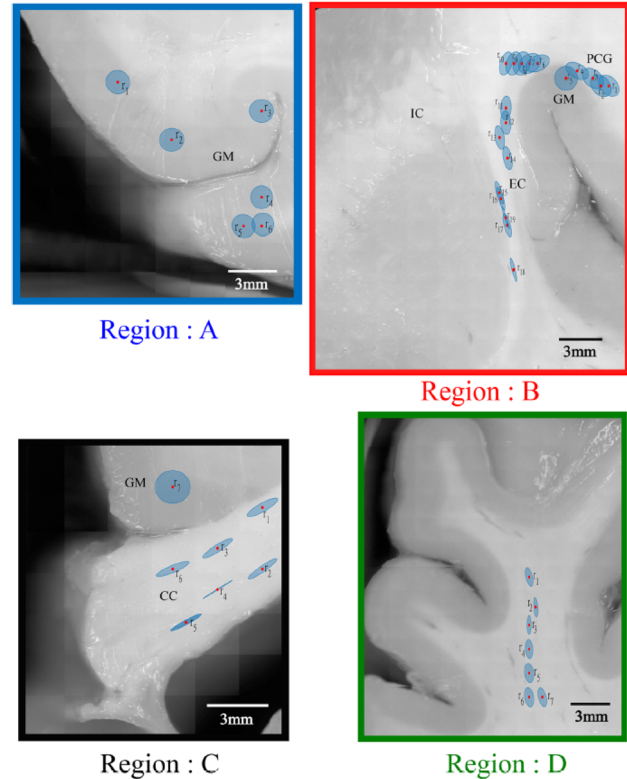

Figure 4: Ellipse-encoded visualization of mean alignment direction and degree of alignment for different measurements points (r_i in regions (A–D)). The ellipses are superimposed on the wide field gray scale image of tissue surface. The red circles represent the position of the probing beam. The orientation of the ellipses encodes the estimated mean alignment direction and the aspect ratio encodes the degree of alignment. For high degree of alignment the ellipse approaches a line, while for zero degree of alignment it becomes a circle (e.g. region: (A). GM, Gray matter; CC, Corpus Callosum; EC, External capsule; IC, Internal capsule and PCG, PRe-Central Gyrus). Note that the length of the ellipse axis can vary from one region to another due to the different scalings. Reprinted with permission from [43]. ©The optical Society.

and brain fibers tracking [57, 58]. Rodríguez-Núñez et al. [58] described the ferro-electric crystal-based wide-field imaging Mueller polarimetric system operating in a visible wavelength range and used it for brain tissue studies (see Figure 5).

Illumination arm of the wide-field imaging Mueller polarimeter contains xenon lamp as an incoherent light source followed by the polarization state generator (PSG) for the modulation of polarization of incident light beam. In this instrument light reflected and scattered by a sample passes through the polarization state analyzer (PSA) in the detection arm that is followed by an interference filter in the detection arm. To perform the multi-spectral measurements from 450 to 700 nm in steps of 50 nm several 40 nm bandpass interference filters with different central
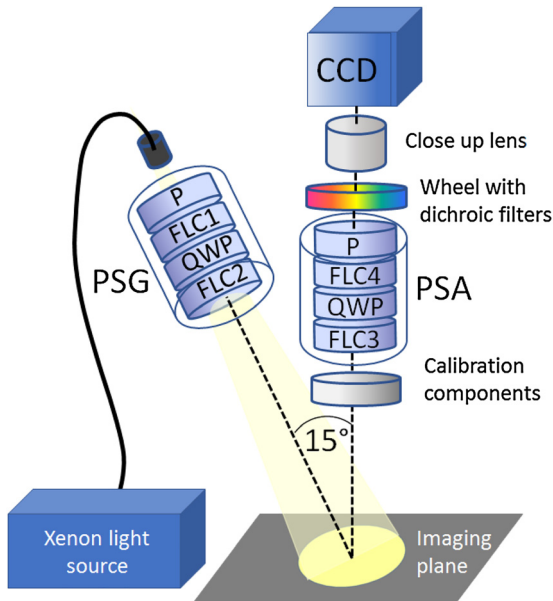
Figure 5: An optical layout of the wide-field imaging Mueller polarimeter. The PSG consists of a linear polarizer *P* followed by a first ferroelectric liquid crystal (FCL1), a quarter-wave plate (QWP) and a second ferroelectric liquid crystal (FLC2). The PSA is assembled from the same optical components in reciprocal configuration.

wavelength were placed in a rotating wheel followed by a CCD camera. The incidence angle of probing light beam is about 15°, the detection is performed at normal angle.

Electrically driven FLCs operate as the wave plates with constant retardation and the orientation of the optical axis that commutes between 0° and 45°. The incident beam is slightly divergent with the diameter of light spot about few cm in the imaging plane. Wide bandpass dichroic filters are used in order to erase speckle pattern. The calibration of the instrument was performed with the eigenvalue calibration method suggested by Compain et al. [11] This method does not require precise modeling of each optical component in both illumination and detection arms and makes use of the dichroic retarders as the reference calibration samples, namely, the polarizer at 0° the polarizer at 90° and a wave plate with the fast axis oriented at 30° in the laboratory reference frame.

At each measurement wavelength 16 intensity images are acquired sequentially by illuminating the sample with four different input polarization states generated by PSG and projecting backscattered light on four different output polarization states of PSA. Using these raw intensity measurements and calibration matrices **W** and **A** the Mueller matrix images of a sample were calculated at each measurement wavelength.

It is worth to mention that there is no straightforward physical interpretation for all elements of Mueller matrix of

an arbitrary sample. The phenomenological approach to Mueller matrix data interpretation consists of decomposing the Mueller matrix of a sample into a sum [59] or a product [14] of Mueller matrices of known optical polarimetric components, namely, diattenuator, retarder and depolarizer. All Mueller matrix decomposition methods make use of certain *a priori* assumptions (e.g. sequential order of polarimetric components [14, 15], low values of polarimetric parameters [60], homogeneity of a sample along the optical path of a probing beam [16, 17], incompleteness of Mueller matrix [61], etc.). The effective values of polarimetric parameters of a sample that were obtained using various decomposition algorithms can be slightly different, however, the corresponding values are quite close when the initial assumptions on the applicability of the decomposition algorithms are obeyed [61].

The wide-field imaging Mueller polarimetry was used for the structural studies of brain and diagnosis of brain diseases as reported in the following subsections.

3.1 Polarimetric staging of Alzheimer's disease in mice model

Due to constant aging of human population the neurodegenerative diseases represent the important challenge for public healthcare system [62, 63] with Alzheimer's disease (AD) accounting for up to 70% of all cases [64]. The most common biomarkers of AD include structural changes of certain brain zones (e.g. the shrinkage of hippocampus) and also an increased extracellular deposition of amyloid-beta Aβ protein and intracellular accumulation of tau protein [65].

The imaging techniques that are currently used in clinic for diagnosis of AD (e.g. MRI, computer tomography scan) and assessment of the results of AD's experimental treatment have relatively low spatial resolution (few hundreds of microns) that prevent them from the accurate detection of abnormal accumulation and deposition of proteins in a brain tissue. Borovkova et al. [56] reported the results of Mueller polarimetric studies of the formalin-fixed paraffin-embedded mice brains from the APP-transgenic mice sacrificed at different age (from 50 to 200 days). The age of animals was correlated with the stage of β-amyloidosis with first deposits of Aβ protein starting at day 45.

Paraffin-embedded halves of mice brains from 21 animals (3 per each time point) were imaged with the wide-field multi-spectral imaging Mueller polarimeter described above in order to check the potential of this optical imaging modality for fast non-contact label-free screening and staging of AD to support the gold standard histology analysis by a pathologist. The Mueller matrix images of a

paraffin block with two halves of brain of a 75-days old mouse that were measured at 450 nm, 500 and 550 nm are shown in Figure 6.

All spectral Mueller matrices are diagonal, which means that the sample behaves as a partial depolarizer at all studied wavelengths. The contrast between the zones of paraffin-embedded mouse brain (two bright spots in the diagonal images) and surrounding paraffin drops with the wavelength increase.

The regions of interest (ROI) corresponding to the zones of mice brain at different time points of AD progression were selected manually in the images recorded at 450 nm. The maps of total depolarization $\Delta = 1 - (|M_{11}| + |M_{22}| + |M_{33}|)/3$ were created and the statistical analysis of the distribution of depolarization values at each time point of AD progression was performed. The main focus of this study was on testing the capabilities of imaging Mueller polarimetry to provide the quantitative metrics for staging of AD and assessing the severity of related brain structural alterations.

The mean value of total depolarization Z_1, the standard deviation Z_2, the skewness Z_3, and the kurtosis Z_4 were calculated for the depolarization maps of all 21 brain samples measured at 450 nm:

$$Z_1 = \frac{1}{N} \sum_{i=1}^{N} \Delta_i \tag{9}$$

$$Z_2 = \sqrt{\frac{1}{N-1} \sum_{i=1}^{N} (\Delta_i - Z_1)^2} \tag{10}$$

$$Z_3 = \frac{1}{Z_2^3} \frac{1}{N} \sum_{i=1}^{N} (\Delta_i - Z_1)^3 \tag{11}$$

$$Z_4 = \frac{1}{Z_2^4} \frac{1}{N} \sum_{i=1}^{N} (\Delta_i - Z_1)^4 \tag{12}$$

where N is the number of pixels in the ROI of the corresponding image. Four statistical moment values were averaged over each age group (see Figure 7).

Whereas both mean value and standard deviation (Eqs. (9) and (10)) of the depolarization distributions do not change
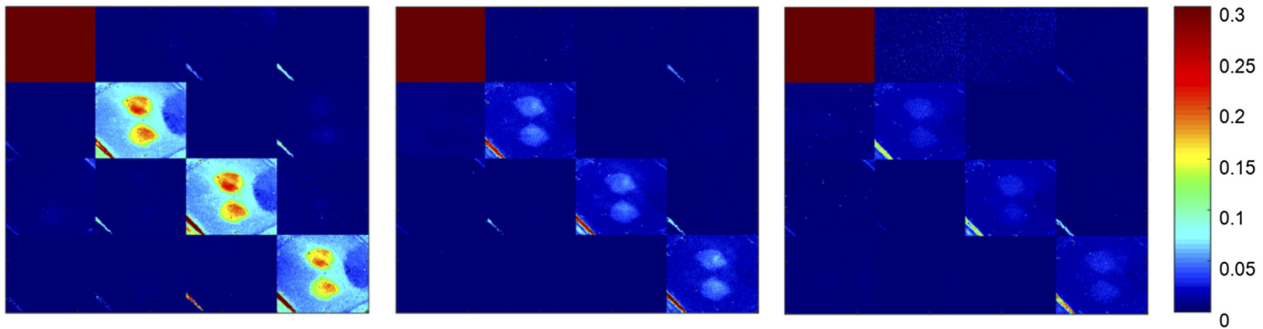

Figure 6: 4×4 Mueller matrix images of an FFPE mouse brain sample (75-days old) measured at 450 nm (left panel), 500 nm (central panel) and 550 nm (right panel). Field of view: 12 mm × 14.5 mm (251 × 301 pixels). Reprinted with permission from [56]. ©The optical Society.
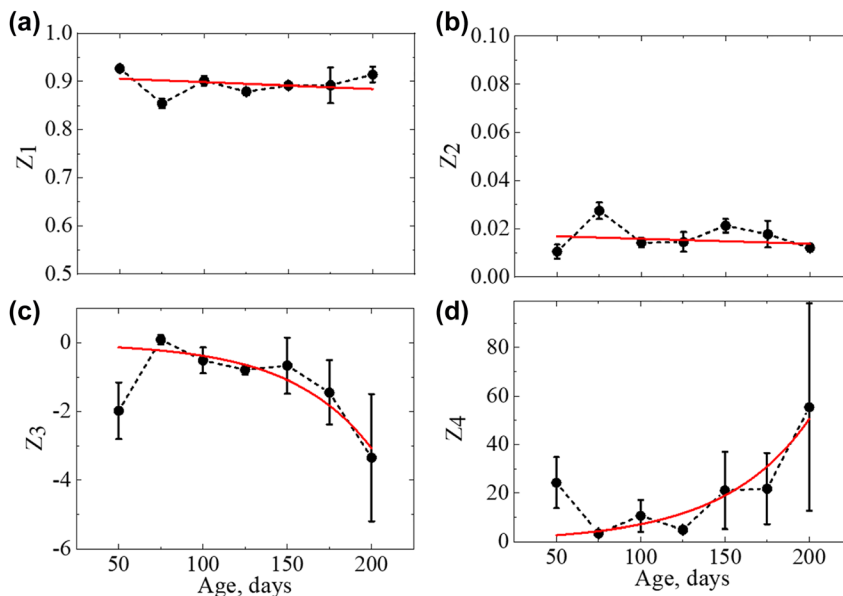

Figure 7: Statistical moments of the 1st to 4th order of the spatial distributions of total depolarization of FFPE mouse brain at different stages of AD development (50–200 days) measured at 450 nm: (a) Mean values, (b) standard deviation, (c) skewness, (d) kurtosis. Results of the fit with (a, b) linear and (c, d), exponential functions are shown by red solid lines. Reprinted with permission from [56]. ©The optical Society.

with the progression of AD (Figure 7a, b), the absolute values of the third and fourth statistical moments (Eqs. (11) and (12)) grow exponentially with AD evolution (Figure 7a, d).

Usually biological tissue is highly scattering and, hence, strongly depolarizing medium. The increase in number density and average size of Aβ-plaques with the progression of AD changes the optical properties of bulk brain tissue by modifying its scattering coefficient μ_s and anisotropy factor g, respectively [66]. However, the value of the reduced scattering coefficient of bulk brain tissue $\mu'_s = \mu_s(1 - g)$ is almost not affected by the simultaneous increase of both parameters μ_s and g.

The distribution of depolarization values becomes skewed towards the lower values with AD progression as confirmed by the negative sign of Z_3 and the increase of its absolute value (see Figure 7c). Exponential increase in the values of kurtosis with the progression of AD (Figure 7d) indicates the exponential growth of the contribution of outliers related to the structural modifications of brain tissue by AD. The increase in effective size of scatterers affects both the scattering cross-section and the angular dependence of a scattering phase function of a scatterer. Compared to Rayleigh scattering regime light scattering within brain tissue becomes more anisotropic with AD progression. The spatial variation of scattering phase function is also enhanced by the increase of the spatial variation of optical refractive index within the bulk of AD brain. Both factors affect the trajectories of multiple scattered photons in terms of the path length, directions and number of scattering events. It results in an increased variability of degree of polarization of the detected photons [67] and explains an increase in absolute values of the skewness and kurtosis of the distribution of depolarization with AD evolution.

The same set of mice brain samples was studied with a scanning Stokes polarimeter at oblique incidence of 50° with respect to a sample surface normal. The backscattered light was detected at the angle of 30° with respect to a sample surface normal and at variable distance from the illuminated point [68]. According to Borovkova et al. [56, 68] the evolution of depolarization parameter with AD progression holds promise to become the quantitative metrics for the optical assessment of β-amyloidosis severity in AD brain diagnosis and staging by a pathologist.

3.2 Brain fiber tracking for assisting neurosurgery

The visualization of the exact border between brain tumor and healthy brain tissue during neurosurgery represents a challenging problem as neurosurgeon looks for the most complete excision of brain tumor while preserving neurological functions. However, the visual contrast between the tumor and healthy brain tissue is very low and it is difficult to determine the limits of infiltrated brain tissue with the white light surgical microscope. The advanced intraoperative imaging techniques that are currently used for tumor visualization (e.g. magnetic resonance imaging [69] and 5-aminolevulinic acid (5-ALA) induced fluorescence imaging [70]) have serious drawbacks in terms of their cost, time budget and sensitivity. Schucht et al. [57] suggested using wide-field imaging Mueller polarimetry to increase the contrast between tumor and healthy brain by detecting the optical anisotropy of healthy brain white matter. The latter is related to the presence of fiber tracts (densely packed bundles of axons) that produce form birefringence of healthy brain white matter. Brain tumor cells grow chaotically and erase the anisotropy of refractive index. This structural difference is not visible with naked eye, but can be detected with polarized light. Thus, the new paradigm of the precise delineation of tumor border during neurosurgery relies on the capability of polarimetric imaging technique to visualize the fiber tracts of surrounding healthy brain tissue.

The multi-spectral wide-field imaging Mueller polarimetric system described in [57] was used for the studies of formalin-fixed human brains in reflection geometry. Two adjacent thick brain sections (~1 cm) in a coronal plane were used for polarimetric imaging and gold standard histology analysis, respectively. The first brain specimen (lateral dimensions ~ 7 cm × 9 cm) was covered by distilled water before imaging to remove the possible impact of uneven cut surface. The Mueller matrix images were recorded at 550 nm. For the physical interpretation of Mueller matrix images the non-linear data compression algorithm, namely, polar decomposition suggested by Lu and Chipman [14] was applied pixel-wise to produce the maps of polarimetric parameters (diattenuation, retardance) and depolarization map. The commercial white light microscope was used by a pathologist to image the whole-mount silver-stained thin section of the second brain section.

The photo of the first brain specimen and corresponding map of the azimuth of the optical axis of uniaxial linear birefringent medium are shown in Figure 8. It is known that white matter of brain tissue exhibits negative birefringence [71]. That is why the in-plane directions of brain fiber tracts are clearly distinguishable in the map of the azimuth of the slow optical axis.

The region of U-fibers connecting neighbor zones of cortex was zoomed in the azimuth map and compared to the histology image of the corresponding zone of silver-stained thin section of brain (see Figure 8, central panels). Visible
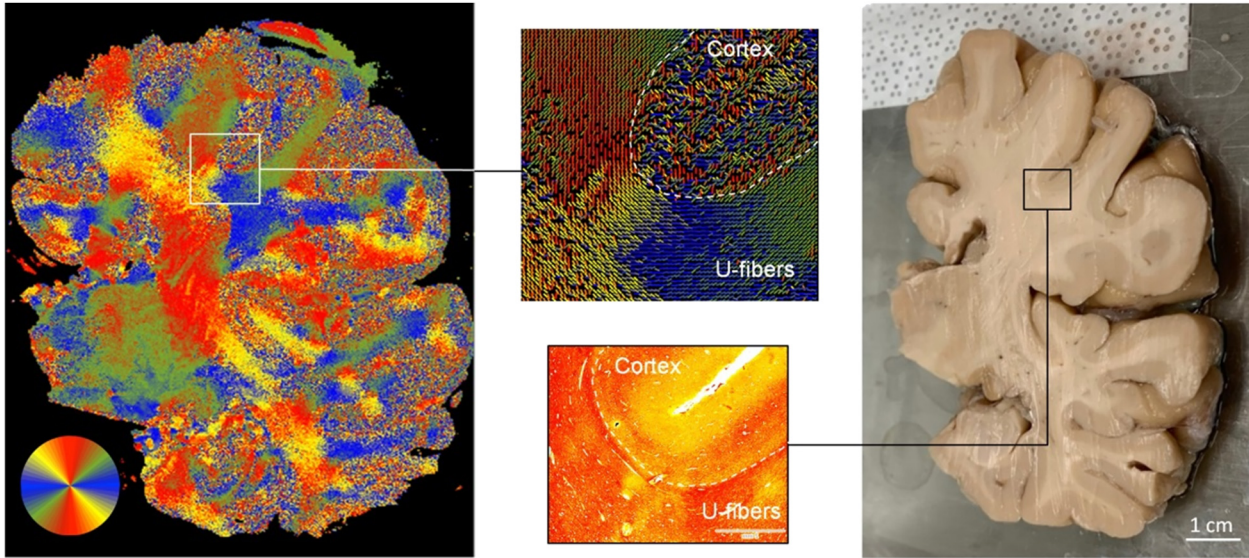
Figure 8: Photo of 1-cm thick section of a formalin-fixed human brain from an anonymous donor (one half) in a coronal plane (right panel); the map of the azimuth of the optical axis measured with wide-field imaging polarimeter at 550 nm (left panel); enlarged U-fibers zone in the map of the azimuth (top central panel); conventional microscopy image of silver-stained thin histological section of corresponding U-fibers zone from the adjacent thick section of brain (scale bar – 2 mm). Adapted from [57].

correlation of the U-fibers directionality is observed in both images. On the other side, the orientation of the azimuth is random in a cortex zone as there are no detected ordered structures at the spatial resolution of wide-field imaging Mueller polarimeter used in this study (~100 μm). The latter is confirmed by the histology image of a cortex zone.

Rodríguez-Núñez et al. [58] reported on using the same system for the detection of white matter fiber tracts in fresh cadaveric animal brains. The goal of these studies was testing the capabilities of the wide-field imaging Mueller polarimetry for 2D brain fiber tracking under the adverse imaging conditions, including complex topography of surgical cavity and presence of blood on the surface of imaged

brain. The temporal lobe and part of the frontal lobe of one hemisphere of fresh cadaveric calf brain were removed with a scalpel to create a 2-cm deep cavity that was imaged with the wide-field imaging Mueller polarimeter and the maps of the polarimetric parameters were generated by applying the Lu-Chipman decomposition of the recorded Mueller matrix images. The photo of a brain hemisphere, the reflected intensity image of the cavity and the corresponding map of the azimuth distribution within the cavity are shown in Figure 9.

No contrast that highlights the directions of white matter fiber tracts is seen in the backscattered intensity image (Figure 9a). Complex topography of cavity's surface leads to the saturation of certain pixels of the intensity
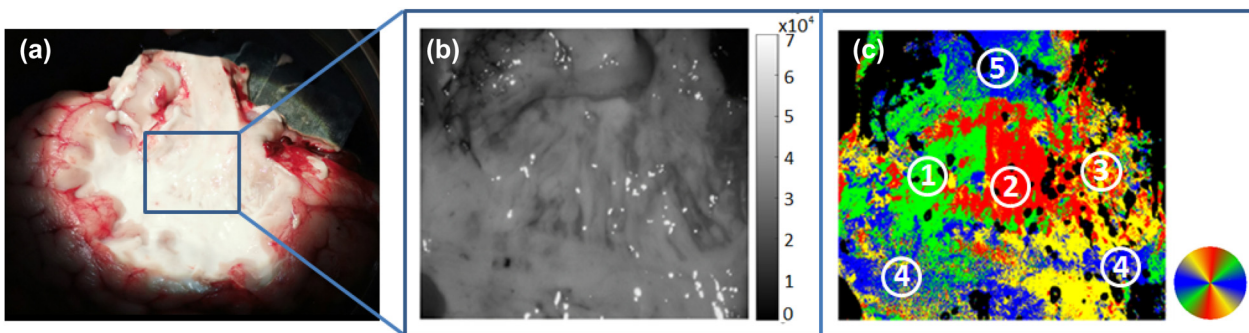

Figure 9: Cerebral tracts of a fresh cadaveric calf brain: (a) Photo of a prepared cavity with brain deep white matter tracts. The imaged zone of the size of 3 cm × 3 cm is marked by a blue box; (b) intensity image; (c) map of the azimuth of the optical axis: the parieto-spinal tract (1) is rendered in green, the centro-spinal tract (2) is rendered in red, the fronto-spinal tract (3) is rendered in yellow, the longitudinal tracts (4) and (5) are rendered in blue. Measurements were performed at 550 nm. Reprinted with permission from [58] ©The optical Society.

image due to specular reflection. All zones with low values of depolarization parameter (<0.85) were excluded from further analysis to remove the impact of specular reflection on azimuth map. The latter visualizes both longitudinal and cerebro-spinal tracts, thus, proving the capability of the wide-field imaging Mueller polarimetry to detect brain fiber tracts in fresh brain tissue (Figure 9c).

The quality of intra-operative visualization of brain fiber tracts with polarized light may be hampered by the presence of blood within surgical cavity. To test the impact of blood on the polarimetric images of brain fiber tracts obtained with the imaging Mueller polarimetric modality Rodríguez-Núñez et al. [58] recorded the multi-spectral Mueller matrix images of a fresh calf brain corpus callosum (a wide thick fiber tract connecting brain hemispheres) that was partially covered by whole blood (see Figure 10a, d).

The intensity image recorded at 550 nm (Figure 10b) demonstrated high contrast between the blood-covered and non-covered zones of a corpus callosum due to the peak of hemoglobin absorption at 550 nm. This contrast is removed in the intensity image taken at 650 nm (Figure 10e), due to the drop of hemoglobin absorption coefficient with wavelength increase towards the red part of a visible spectrum.

The maps of the azimuth measured at both 550 and 650 nm show vertical orientation of fiber tracts in the imaging plane for the zones of corpus callosum that were not covered by blood. At 550 nm the azimuth of the optical axis is randomized within the blood-covered zone due to the strong blood hemoglobin absorption (Figure 10c). This effect is almost eliminated for the azimuth map measured at 650 nm (Figure 10f).

These results support the assumption that presence of blood (usually diluted with a saline solution used during surgery for rinsing) within a surgical cavity will not affect the performance of the fiber tracts detection in the tissue-at-sight during neurosurgery with the wide-field imaging Mueller polarimetry.

It was shown that machine learning approach (ML) can enhance the contrast in polarimetric images of tissue at micro-scale [72, 73] and also help the diagnostic interpretation of the wide-field polarimetric images of brain tissue [74].

4 Summary

In this concise review we have summarized the work of various research groups on optical studies of brain tissue using different polarimetric imaging techniques. This approach has demonstrated great potential for structural and diagnostic studies of brain tissue. The latest advances
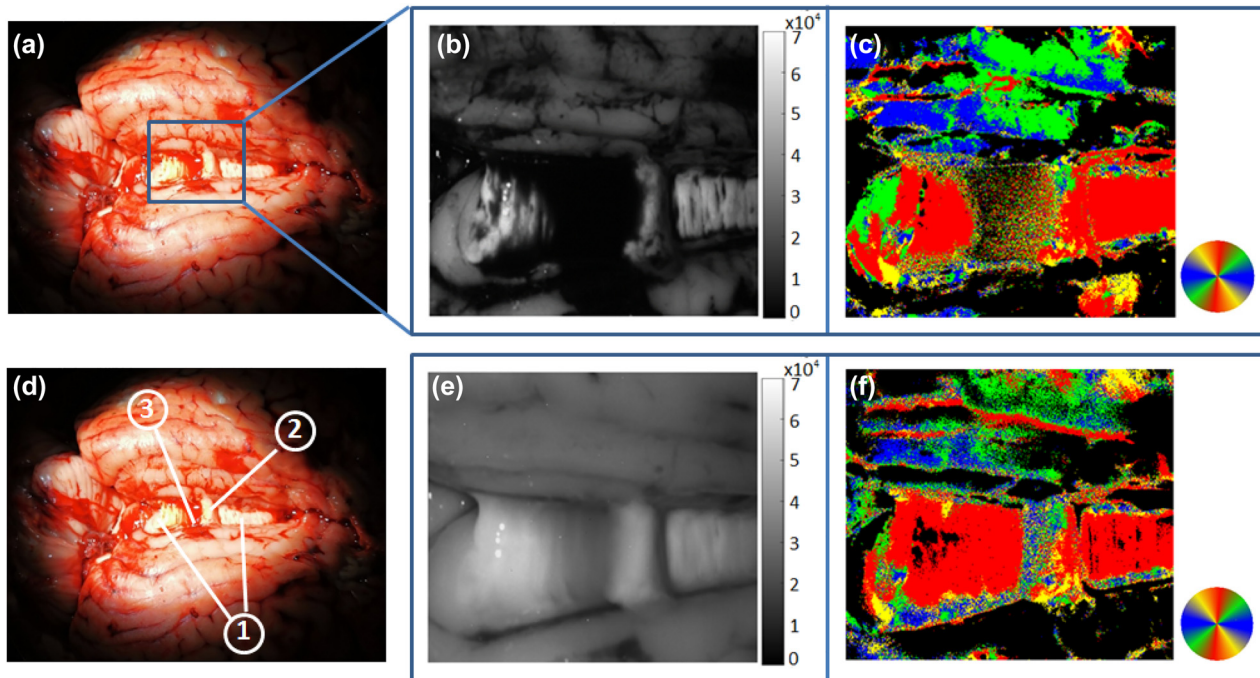

Figure 10: Images of the corpus callosum in a cadaveric calf brain with a 2 mm deep pool of 100% blood: (a) color photo; (b) intensity image; (c) azimuth of the optical axis measured at 550 nm; (d) corpus callosum (1) with a 2 mm thick tissue specimen (2) creating a 2 mm deep pool filled with whole blood (3); (e) intensity image and (f) azimuth of the optical axis measured at 650 nm. Reprinted with permission from [58] ©The optical Society.

in this field include reconstruction of brain connectome, visualization of in-plane brain fiber tracts for brain tumor contrast increase during neurosurgery, histopathology analysis for staging the Alzheimer's disease.

The potential of the multi-scale 3D-PLI modality to determine the three-dimensional course of nerve fibers in gross histological sections of brain with in-plane resolution of few tens of micrometers was discussed together with the developments to address the challenges of tracking crossing nerve fibers and detecting out-of-plane fiber inclination angle. The complementary numerical modeling helped to better understand and interpret the influence of various crossing fiber spatial arrangement on the measured signal of 3D PLI modality.

Different polarimetric techniques operating in reflection mode were also discussed. The polarimetric microscope that provides data on the components of Stokes vector was used for the analysis of anisotropic structure of different regions in thick coronal section of a formalin-fixed human brain. With this polarimetric imaging modality it was possible to measure the local birefringence exhibited by brain white matter, and relate it to the in-plane orientation of fiber tracts and the degree of fiber tract alignment.

The wide-field multi-spectral imaging complete Mueller matrix polarimetry was also discussed. This polarimetric imaging modality demonstrated its potential for optical diagnosis of brain tissue including the fast non-contact and label-free screening and staging of Alzheimer's disease to support the histology analysis by a pathologist and brain fibers tracking in both formalin-fixed and fresh brain specimens targeting real-time delineation of brain tumor that currently represents a major challenge in neurosurgery.

The results obtained with polarimetric imaging techniques advance our understanding of brain structural properties and optical diagnosis of brain tissue and demonstrate that brain polarimetry is an actively developing field of research. Reducing the acquisition time and the number of necessary polarimetric measurements without sacrificing important polarimetric information is a main challenge that can be addressed by developing an adaptive polarimetry and devising most appropriate data reduction algorithms for brain characterization. The studies discussed in this review are opening the avenue for the implementation of optical polarimetric techniques into clinical practice.

References

[1] R. M. A. Azzam, "Stokes-vector and Mueller-matrix polarimetry," *J. Opt. Soc. Am.*, vol. 33, no. 7, pp. 1396–1408, July 2016.

[2] M. Born and E. Wolf, *Principles of Optics*, 7th ed. Cambridge, UK, Cambridge University Press, 1999.

[3] D. Goldstein, *Polarized Light*, 2nd ed. New York, Marcel Dekker, 2003.

[4] G. G. Stokes, "On the change of refrangibility of light," *Phil. Trans. R. Soc. London*, vol. 142, pp. 463–562, 1952.

[5] R. A. Chipman, "Chapter 22: polarimetry," in *Handbook of Optics Volume II: Devices, Measurements, and Properties*, 2nd ed. M. Bass, Ed., New York, USA, McGraw-Hill, 2009.

[6] H. Mueller, *"Memorandum on the Polarization Optics of the Photoelastic Shutter," Report No. 2 of the OSRD Project OEMsr*, 1943, p. 576.

[7] J. L. Pezzanti and R. A. Chipman, "Mueller matrix scatter polarimetry of a diamond-turned mirror," *Opt. Eng.*, vol. 34, pp. 1593–1598, 1995.

[8] R. W. Collins and J. Koh, "Dual rotating-compensator multichannel ellipsometer: instrument design for real-time Mueller matrix spectroscopy of surfaces and films," *J. Opt. Soc. Am. A*, vol. 16, pp. 1997–2006, 1999.

[9] F. Delplancke, "Automated high-speed Mueller matrix scatterometer," *App. Opt.*, vol. 36, pp. 5388–5395, 1997.

[10] G. E. Jellison and F. A. Modine, "Two-modulator generalized ellipsometry: experiment and calibration," *Appl. Opt.*, vol. 36, pp. 8184–8189, 1997.

[11] E. Compain, S. Poirier, and B. Drévillon, "General and self-consistent method for the calibration of polarization modulators, polarimeters, and Mueller-matrix ellipsometers," *Rev. Sci. Instrum.*, vol. 38, pp. 3490–3502, 1998.

[12] J. S. Tyo and T. S. Turner, "Imaging spectropolarimeters for use in visible and infrared remote sensing," *Proc. SPIE*, vol. 3753, 1999, Imaging Spectrometry V. https://doi.org/10.1117/12.366312.

[13] J. M. Bueno and P. Artal, "Double-pass imaging polarimetry in the human eye," *Opt. Lett.*, vol. 24, pp. 64–66, 1999.

[14] S. Y. Lu and R. A. Chipman, "Interpretation of Mueller matrices based on polar decomposition," *J. Opt. Soc. Am. A*, vol. 13, pp. 1106–1113, 1996.

[15] J. Morio and F. Goudail, "Influence of the order of diattenuator, retarder, and polarizer in polar decomposition of Mueller matrices," *Opt. Lett.*, vol. 29, pp. 2234–2236, 2004.

[16] R. Ossikovski, "Differential matrix formalism for depolarizing anisotropic media," *Opt. Lett.*, vol. 36, pp. 2330–2332, 2011.

[17] V. Devlaminck, "Depolarizing differential Mueller matrix of homogeneous media under Gaussian fluctuation hypothesis," *J. Opt. Soc. Am. A*, vol. 32, pp. 1736–1743, 2015.

[18] W. J. Schmidt, *Die Bausteine des Tierkörpers im polarisierten Lichte*, Bonn, Cohen, 1924.

[19] G. Scheuner and J. Hutschenreiter, *Polarisationsmikroskopie in der Histophysik*, Leipzig, Thieme, 1972.

[20] M. Wolman, "Polarized light microscopy as a tool of diagnostic pathology," A review, *J. Histochem. Cytochem.*, vol. 23, pp. 21–50, 1975.

[21] H. J. Kretschmann, "On the demonstration of myelinated nerve fibers by polarized light without extinction effects," *J. Hirnforsch.*, vol. 9, pp. 571–575, 1967.

[22] J. P. Fraher and M. A. MacConaill, "Fiber bundles in the CNS revealed by polarized light," *J. Anat.*, vol. 170, p. 106, 1970.

[23] H. Axer, B. E. Lippitz, and D. Gv. Keyserlingk, "Morphological asymmetry in anterior limb of human internal capsule revealed by confocal laser and polarized light microscopy," *Psychiatry Res. Neuroimaging.*, vol. 91, pp. 141–154, 1999a.

[24] H. Axer, M. Axer, T. Krings, and D. Gv. Keyserlingk, "Quantiative estimation of 3-D fiber course in gross histological sections of the human brain using polarized light," *J. Neourosci. Methods*, vol. 105, pp. 121–131, 2001.

[25] H. Axer and D. Gv. Keyserlingk, "Mapping of fiber orientation in human internal capsule by means of polarized light and confocal scanning laser microscopy," *J. Neurosci. Methods*, vol. 94, pp. 165–175, 2000.

[26] C. Brosseau, *Polarized light - a Statistical Optics Approach*, New York, Wiley, 1998.

[27] M. Axer, K. Amunts, D. Grässel, et al., "A novel approach to the human connectome: Ultra-high resolution mapping of fiber tracts in the brain," *Neuroimage*, vol. 54, pp. 1091–1101, 2011.

[28] R. C. Jones, "A new calculus for the treatment of optical systems," *J. Opt. Soc. Am.*, vol. 31, pp. 488–503, 1941.

[29] S. Mori, B. J. Crain, V. P. Chacko, and P. C. Zijl, "Three-dimensional tracking of axonal projections in the brain by magnetic resonance imaging," *Ann. Neurol.*, vol. 45, pp. 265–269, 1999.

[30] H. Axer, L. Mattthias, M. Mürköster, et al., "A 3D fiber model of the human brainstem," *Comput. Med. Imaging Graph.*, vol. 26, pp. 439–444, 2002.

[31] L. Larsen, L. D. Griffin, D. Gräbel, O. W. Witte, and H. Axer, "Polarized light imaging of white matter architecture," *Microsc. Res. Tech.*, vol. 70, pp. 851–863, 2007.

[32] M. Axer, H. Axer, D. Gräßel, K. Amunts, K. Zilles, and U. Pietrzyk, "Nerve fiber "mapping of the human visual cortex using polarized light imaging (PLI)," *IEEE Nucl Sci Symp Conf Rec*, vol. 1, 2007, 4244-0923-3/07. https://doi.org/10.1109/nssmic.2007.4437076.

[33] S. Mori and J. Zhang, "Principles of diffusion tensor imaging and its applications to basic neuroscience research," *Neuron*, vol. 5, pp. 527–539, 2006.

[34] D. S. Tuch, T. G. Teese, M. R. Wiegell, N. Makris, J. W. Belliveau, and V. J. Wedeen, "High angular resolution diffusion imaging reveals intravoxel white matter fiber heterogeneity," *Magn. Reson. Med.*, vol. 48, pp. 577–582, 2002.

[35] U. Türe, M. G. Yasargil, A. H. Friedmann, and O. Al-Mefty, "Fiber dissection technique: lateral aspect of the brain," *Neurosurgery*, vol. 47, pp. 417–427, 2000.

[36] U. Bürgel, I. Mecklenburg, U. Blohm, and K. Ziles, "Histological visualization of long fiber tracts in the white matter of adult human brains," *J. Brain Res.*, vol. 38, pp. 397–404, 1997.

[37] U. Bürgel, K. Amunts, L. Hoemke, H. Mohlberg, J. M. Gilsbach, and K. Zilles, "White matter fiber tracts of the human brain: three-dimensional mapping at microscopic resolution, topography and intersubject variability," *Neuroimage*, vol. 29, pp. 1092–1105, 2006.

[38] M. Axer, D. Grässel, M. Kleiner, et al., "High-resolution fiber tract reconstruction in the human brain by means of three-dimensional polarized light imaging," *Front Neuroinform.*, vol. 5, p. 34, 2011.

[39] H. Axer, C. M. Klingner, and A. Prescher, "Fiber anatomy of dorsal and ventral language streams," *Brain Lang.*, vol. 127, no. 2, pp. 192–204, 2012.

[40] M. Menzel, K. Michielsen, H. De Raedt, J. Reckfort, K. Amunts, and M. Axer, "A Jones matrix formalism for simulating three-dimensional polarized light imaging of brain tissue," *J. R. Soc. Interface*, vol. 12, 2015, 20150734. https://doi.org/10.1098/rsif.2015.0734.

[41] M. Dohmen, M. Menzel, H. Wiese, et al., "Understanding fiber mixture by simulations in 3D polarized light imaging," *Neuroimage*, vol. 1 11, pp. 464–475, 2015.

[42] D. Schmitz, K. Amunts, T. Lippert, and M. Axer, "A least squares approach for the reconstruction of nerve fiber orientations from tiltable specimen experiments in 3D-PLI," in *2018 IEEE 15th International Symposium on Biomedical Imaging (ISBI)*, Washinton, DC, USA, 2018, pp. 132–135.

[43] A. Jain, L. Ulrich, M. Jaeger, P. Shucht, M. Frenz, and H. Günhan Akarkay, "Backscattering polarimetric imaging of the human brain to determine the orientation and degree of alignment of nerve fiber bundles," *Biomed. Opt Express*, vol. 12, pp. 4452–4466, 2021.

[44] M. Hornung, A. Jain, M. Frenz, and H. Günhan Akarcay, "Interpretation of backscattering polarimetric images recorded from multiply scattering systems: a study on colloidal suspensions," *Opt Express*, vol. 27, no. 5, pp. 6210–6639, 2019.

[45] A. Jain, A. K. Maurya, L. Ulrich, et al., "Polarimetric imaging in backscattering for the structural characterization of strongly scattering birefringent fibrous media," *Biomed. Opt Express*, vol. 28, pp. 16673–16695, 2020.

[46] S. Ben Hatit, *Polarimétrie de Mueller résolue en angle*, PhD thesis, Palaiseau, France, Ecole Polytechnique, 2009.

[47] C. Fallet, T. Novikova, M. Foldyna, et al., "Overlay measurements by Mueller polarimetry in back focal plane," *J. Microlithogr, Microfabr, Microsyst.*, vol. 10, 2011, Art no. 033017.

[48] O. Korotkova and D. James, "Definitions of the degree of polarization of a light," *Opt. Lett.*, vol. 32, pp. 1015–1016, 2007.

[49] K. Oishi, A. V. Faria, P. C. M. van Zijl, et al., *MRI Atlas of Human White Matter*, 2nd ed. Cambridge, Massachusetts, USA, Academic Press, 2010.

[50] K. Zilles, N. Palomero-Gallagher, D. GräBel, et al., "Chapter 18 - high-resolution fiber and fiber tract imaging using polarized light microscopy in the human, monkey, rat, and mouse brain," in *Axons and Brain Architecture*, K. S. Rockland, Ed., San Diego, Academic Press, 2016, pp. 369–389.

[51] A. Pierangelo, A. Nazac, A. Benali, et al., "Polarimetric imaging of uterine cervix: a case study," *Opt Express*, vol. 21, no. 12, pp. 14120–14130, 2013.

[52] M. Kupinski, M. Boffety, F. Goudail, et al., "Polarimetric measurement utility for pre-cancer detection from uterine cervix specimens," *Biomed. Opt Express*, vol. 25, no. 11, pp. 5691–5702, 2018.

[53] A. Pierangelo, S. Manhas, A. Benali, et al., "Use of Mueller polarimetric imaging for the staging of human colon cancer," *Proc. SPIE Optical Biopsy.*, vol. IX, no. 7895, p. 78950E, 2011.

[54] T. Novikova, J. Rehbinder, H. Haddad, et al., "Multi-spectral Mueller matrix imaging polarimetry for studies of human tissue,"

OSA Biophotonics Congress, Clinical and Translational Biophotonics, paper TTh3B, 2016, https://doi.org/10.1364/TRANSLATIONAL.2016.TTh3B.2.

[55] J. Chue-Sang, N. Holness, M. Gonzalez, et al., "Use of Mueller matrix colposcopy in the characterization of cervical collagen anisotropy," *J. Biomed. Opt.*, vol. 2312, p. 121605, 2018.

[56] M. Borovkova, A. Bykov, A. Popov, et al., "Evaluating β-amyloidosis progression in Alzheimer's disease with Mueller polarimetry," *Biomed. Opt Express*, vol. 11, no. 8, pp. 4509–4519, 2020.

[57] P. Schucht, H. R. Lee, M. H. Mezouar, et al., "Visualization of white matter fiber tracts of brain tissue sections with wide-field imaging Mueller polarimetry," *IEEE Trans. Med. Imaging*, vol. 39, no. 12, pp. 4376–4382, 2020.

[58] O. Rodriguez-Nunez, P. Schucht, E. Hewer, T. Novikova, and A. Pierangelo, "Polarimetric visualization of healthy brain fiber tracts in adverse conditions: ex vivo studies," *Biomed. Opt Express*, vol. 12, no. 10, pp. 6674–6685, 2021.

[59] S. R. Cloude, "Group theory and polarisation algebra," *Optik*, vol. 75, pp. 26–36, 1986.

[60] S. Bancelin, A. Nazac, B. Haj Ibrahim, et al., "Determination of collagen fiber orientation in histological slides using Mueller microscopy and validation by second harmonic generation imaging," *Opt Express*, vol. 22, no. 19, pp. 22561–22574, 2014.

[61] M. Gonzalez, R. Ossikovski, T. Novikova, and J. C. Ramella-Roman, "Introduction of a 3×4 Mueller matrix decomposition method," *J. Phys. D Appl. Phys.*, vol. 54, no. 42, p. 424005 (1–9), 2021.

[62] V. L. Feigin and T. Vos, "Global burden of neurological disorders: from global burden of disease estimates to actions," *Neuroepidemiology*, vol. 52, pp. 1–2, 2019.

[63] G. Deuschl, E. Beghi, and F. Fazekas, "The burden of neurological diseases in Europe: an analysis for the global Burden of disease study 2017," *Lancet*, vol. 5, no. 10, pp. E551–E567, 2020.

[64] World Health Organization WHO, 2021. https://www.who.int/news-room/fact-sheets/detail/dementia.

[65] H. Braak and E. Braak, "Alzheimer's disease: Striatal amyloid deposits and neurofibrillary changes," *J. Neuropathol. Exp. Neurol.*, vol. 49, no. 3, pp. 215–224, 1990.

[66] C. F. Bohren and D. R. Huffman, *Absorption and Scattering of Light by Small Particles*, John Wiley & Sons, 2008.

[67] N. G. Khlebtsov, I. L. Maksimova, I. Meglinski, L. V. Wang, V. V. Tuchin, "Introduction to light scattering by biological objects: extinction and scattering of light in Disperse Systems," in *Handbook of Optical Biomedical Diagnostics*, V. Tuchin, Ed., Bellingham, Washington, USA, SPIE Press, 2016, Ch. 1.

[68] M. Borovkova, O. Sieryi, I. Lopushenko, et al., "Screening of Alzheimer's disease with multiwavelength Stokes polarimetry in a mouse model," *IEEE Trans. Med. Imaging*, vol. 41, no. 4, pp. 977–982, 2022.

[69] C. M. Rogers, P. S. Jones, and J. S. Weinberg, "Intraoperative MRI for brain tumors," *J. Neuro Oncol.*, vol. 151, pp. 479–490, 2021.

[70] P. Schucht, S. Knittel, J. Slotboom, et al., "5-ALA complete resections go beyond MR contrast enhancement: Shift corrected volumetric analysis of the extent of resection in surgery for glioblastoma," *Acta Neurochir.*, vol. 156, no. 2, pp. 305–312, 2015.

[71] M. Menzel, M. Axer, K. Amunts, H. De Raedt, and K. Michielsen, "Diattenuation Imaging reveals different brain tissue properties," *Sci. Rep.*, vol. 9, p. 1939, 2019.

[72] L. Si, N. Li, T. Huang, et al., "Computational image translation from Mueller matrix polarimetry to bright-field microscopy," *J. Biophotonics*, vol. 15, 2022, Art no. e202100242.

[73] M. Gonzalez, C. Roa, A. Jimenez, et al., "Machine learning powered Mueller matrix microscope for collagen and elastin visualization in the mouse cervix"," in *Proc. SPIE Polarized Light and Optical Angular Momentum for Biomedical Diagnostics*, 2022, p. 119630B. 11963.

[74] R. I. McKinley, L. A. Felger, E. Hewer, et al., "Machine learning for white matter fibre tract visualization in the human brain via Mueller matrix polarimetric data," *Proc. SPIE Unconventional Optical Imaging III*, vol. 12136, p. 121360G, 2022.